

COPYRIGHT NOTICE

© 2018 Optical Society of America.

Users may use, reuse, and build upon the article, or use the article for text or data mining, so long as such uses are for non-commercial purposes and appropriate attribution is maintained.

All other rights are reserved.

High throughput detection chain for time domain optical mammography

EDOARDO FEROCINO,^{1,*} EDOARDO MARTINENGI,¹ ALBERTO DALLA MORA,¹ ANTONIO PIFFERI,^{1,2} RINALDO CUBEDDU,¹ AND PAOLA TARONI^{1,2}

¹Politecnico di Milano, Department of Physics, Piazza Leonardo da Vinci, 32, 20133, Milan, Italy

²CNR-Istituto di Fotonica e Nanotecnologie, Piazza Leonardo da Vinci, 32, 20133, Milan, Italy

*edoardo.ferocino@polimi.it

Abstract: A novel detection chain, based on 8 Silicon Photomultipliers (forming a wide-area custom-made detection probe) and on a time-to-digital converter, was developed to improve the signal level in multi-wavelength (635-1060 nm) time domain optical mammography. The performances of individual components and of the overall chain were assessed using established protocols (BIP and MEDPHOT). The photon detection efficiency was improved by up to 3 orders of magnitude, and the maximum count rate level was increased by a factor of 10 when compared to the previous system, based on photomultiplier tubes and conventional time-correlated single-photon counting boards. In the estimate of optical parameters, the novel detection chain provides performances comparable to the previous system, widely validated in clinics, but with higher signal level, higher robustness, and at a lower price per channel, thus targeting important requirements for clinical applications.

© 2018 Optical Society of America under the terms of the [OSA Open Access Publishing Agreement](#)

OCIS codes: (030.5260) Photon counting; (040.6070) Solid state detectors; (170.6510) Spectroscopy, tissue diagnostics; (170.3830) Mammography; (170.6920) Time-resolved imaging; (170.5280) Photon migration.

References and links

1. T. Durduran, R. Choe, W. B. Baker, and A. G. Yodh, "Diffuse optics for tissue monitoring and tomography," *Rep. Prog. Phys.* **73**(7), 076701 (2010).
2. W. Becker, *Advanced Time-Correlated Single Photon Counting Techniques* (Springer, 2005), Vol. 81.
3. W. Becker, *The Bh TCSPC Handbook*, 7th ed. (2017).
4. D. Grosenick, H. Rinneberg, R. Cubeddu, and P. Taroni, "Review of optical breast imaging and spectroscopy," *J. Biomed. Opt.* **21**(9), 091311 (2016).
5. D. R. Leff, O. J. Warren, L. C. Enfield, A. Gibson, T. Athanasiou, D. K. Patten, J. Hebden, G. Z. Yang, and A. Darzi, "Diffuse optical imaging of the healthy and diseased breast: A systematic review," *Breast Cancer Res. Treat.* **108**(1), 9–22 (2008).
6. D. R. Busch, R. Choe, T. Durduran, and A. G. Yodh, "Towards non-invasive characterization of breast cancer and cancer metabolism with diffuse optics," *PET Clin.* **8**(3), 345–365 (2013).
7. P. C. Pearlman, A. Adams, S. G. Elias, W. P. T. M. Mali, M. A. Viergever, and J. P. W. Pluim, "Mono- and multimodal registration of optical breast images," *J. Biomed. Opt.* **17**(8), 080901 (2012).
8. R. Choe and T. Durduran, "Diffuse Optical Monitoring of the Neoadjuvant Breast Cancer Therapy," *IEEE J. Sel. Top. Quantum Electron.* **18**(4), 1367–1386 (2012).
9. Q. Zhu, L. Wang, S. Tannenbaum, A. Ricci, Jr., P. DeFusco, and P. Hegde, "Pathologic response prediction to neoadjuvant chemotherapy utilizing pretreatment near-infrared imaging parameters and tumor pathologic criteria," *Breast Cancer Res.* **16**(5), 456–469 (2014).
10. D. Grosenick, K. T. Moesta, M. Möller, J. Mücke, H. Wabnitz, B. Gebauer, C. Stroszczynski, B. Wassermann, P. M. Schlag, and H. Rinneberg, "Time-domain scanning optical mammography: I. Recording and assessment of mammograms of 154 patients," *Phys. Med. Biol.* **50**(11), 2429–2449 (2005).
11. P. Taroni, A. Pifferi, E. Salvagnini, L. Spinelli, A. Torricelli, and R. Cubeddu, "Seven-wavelength time-resolved optical mammography extending beyond 1000 nm for breast collagen quantification," *Opt. Express* **17**(18), 15932–15946 (2009).
12. J. C. Hebden, H. Veenstra, H. Dehghani, E. M. C. Hillman, M. Schweiger, S. R. Arridge, and D. T. Delpy, "Three-dimensional time-resolved optical tomography of a conical breast phantom," *Appl. Opt.* **40**(19), 3278–3287 (2001).
13. G. Quarto, L. Spinelli, A. Pifferi, A. Torricelli, R. Cubeddu, F. Abbate, N. Balestreri, S. Menna, E. Cassano, and P. Taroni, "Estimate of tissue composition in malignant and benign breast lesions by time-domain optical mammography," *Biomed. Opt. Express* **5**(10), 3684–3698 (2014).
14. P. Taroni, G. Quarto, A. Pifferi, F. Abbate, N. Balestreri, S. Menna, E. Cassano, and R. Cubeddu, "Breast tissue

- composition and its dependence on demographic risk factors for breast cancer: non-invasive assessment by Time Domain diffuse optical spectroscopy," *PLoS One* **10**(6), e0128941 (2015).
15. P. Taroni, G. Quarto, A. Pifferi, F. Ieva, A. M. Paganoni, F. Abbate, N. Balestreri, S. Menna, E. Cassano, and R. Cubeddu, "Optical identification of subjects at high risk for developing breast cancer," *J. Biomed. Opt.* **18**(6), 060507 (2013).
 16. A. Pifferi, D. Contini, A. D. Mora, A. Farina, L. Spinelli, and A. Torricelli, "New frontiers in time-domain diffuse optics, a review," *J. Biomed. Opt.* **21**(9), 091310 (2016).
 17. A. D. Mora, E. Martinenghi, D. Contini, A. Tosi, G. Boso, T. Durduran, S. Arridge, F. Martelli, A. Farina, A. Torricelli, and A. Pifferi, "Fast silicon photomultiplier improves signal harvesting and reduces complexity in time-domain diffuse optics," *Opt. Express* **23**(11), 13937–13946 (2015).
 18. E. Martinenghi, L. Di Sieno, D. Contini, M. Sanzaro, A. Pifferi, and A. Dalla Mora, "Time-resolved single-photon detection module based on silicon photomultiplier: A novel building block for time-correlated measurement systems," *Rev. Sci. Instrum.* **87**(7), 073101 (2016).
 19. F. Villa, R. Lussana, D. Bronzi, S. Tisa, A. Tosi, F. Zappa, A. Dalla Mora, D. Contini, D. Durini, S. Weyers, and W. Brockherde, "CMOS imager with 1024 SPADs and TDCs for single-photon timing and 3-D time-of-flight," *IEEE J. Sel. Top. Quantum Electron.* **20**(6), 3804810 (2014).
 20. H. Wabnitz, D. R. Taubert, M. Mazurenka, O. Steinkellner, A. Jelzow, R. Macdonald, D. Milej, P. Sawosz, M. Kacprzak, A. Liebert, R. Cooper, J. Hebden, A. Pifferi, A. Farina, I. Bargigia, D. Contini, M. Caffini, L. Zucchelli, L. Spinelli, R. Cubeddu, and A. Torricelli, "Performance assessment of time-domain optical brain imagers, part 1: basic instrumental performance protocol," *J. Biomed. Opt.* **19**(8), 086010 (2014).
 21. A. Pifferi, A. Torricelli, A. Bassi, P. Taroni, R. Cubeddu, H. Wabnitz, D. Grosenick, M. Möller, R. Macdonald, J. Swartling, T. Svensson, S. Andersson-Engels, R. L. P. van Veen, H. J. C. M. Sterenborg, J.-M. Tualle, H. L. Nghiem, S. Avrillier, M. Whelan, and H. Stamm, "Performance assessment of photon migration instruments: the MEDPHOT protocol," *Appl. Opt.* **44**(11), 2104–2114 (2005).
 22. B. A. Dolgoshein, V. Balagura, P. Z. Buzhan, M. V. Danilov, L. A. Filatov, E. Garutti, M. Groll, A. L. Ilyin, V. A. Kantserov, V. A. Kaplin, A. I. Karakash, F. F. Kayumov, S. N. Klemm, V. Korbel, H. J. Meyer, R. V. Mizuk, V. L. Morgunov, E. G. Novikov, P. N. Pakhlov, E. V. Popova, V. Y. Rusinov, F. Sefkow, E. Tarkovsky, and I. N. Tikhomirov, "Status report on silicon photomultiplier development and its applications," *Nucl. Instruments Methods Phys. Res. Sect. A Accel. Spectrometers, Detect. Assoc. Equip.* **563**(2), 368–376 (2006).
 23. E. Martinenghi, A. Dalla Mora, D. Contini, A. Farina, F. Villa, A. Torricelli, and A. Pifferi, "Spectrally Resolved Single-Photon Timing of Silicon Photomultipliers for Time-Domain Diffuse Spectroscopy," *IEEE Photonics J.* **7**(4), 6802512 (2015).
 24. A. D. Mora, D. Contini, S. Arridge, F. Martelli, A. Tosi, G. Boso, A. Farina, T. Durduran, E. Martinenghi, A. Torricelli, and A. Pifferi, "Towards next-generation time-domain diffuse optics for extreme depth penetration and sensitivity," *Biomed. Opt. Express* **6**(5), 1749–1760 (2015).
 25. S. Konugolu Venkata Sekar, A. Dalla Mora, I. Bargigia, E. Martinenghi, C. Lindner, P. Farzam, M. Pagliazzi, T. Durduran, P. Taroni, A. Pifferi, and A. Farina, "Broadband (600-1350 nm) Time-Resolved Diffuse Optical Spectrometer for Clinical Use," *IEEE J. Sel. Top. Quantum Electron.* **22**(3), 7100609 (2016).
 26. A. Pifferi, A. Torricelli, P. Taroni, D. Comelli, A. Bassi, and R. Cubeddu, "Fully automated time domain spectrometer for the absorption and scattering characterization of diffusive media," *Rev. Sci. Instrum.* **78**(5), 053103 (2007).
 27. R. Cubeddu, A. Pifferi, P. Taroni, A. Torricelli, and G. Valentini, "Experimental test of theoretical models for time-resolved reflectance," *Med. Phys.* **23**(9), 1625–1633 (1996).

1. Introduction

Diffuse Optics (DO) is the study of light propagation into strongly diffusive media. It has been largely investigated for imaging and spectroscopy of biological tissues as it enables the non-invasive assessment of tissue absorption (associated to chemical composition) and scattering (associated to microstructure).

When light is injected into a tissue, both absorption and scattering affect the photon trajectories from the light source to the detector. Thus, to study the optical properties and derive information on the composition and structure of the biological medium, the decoupling of scattering from absorption effects is needed. The Time Domain (TD) approach to DO can efficiently separate the contributions of scattering and absorption with a single measure [1] by studying the attenuation, delay and broadening of a short light pulse diffused through the tissue. TD measurements are often performed through the Time-Correlated Single-Photon Counting (TCSPC) technique, thanks to its ability to acquire fast and weak signals [2] that are typical of the TD methods.

A common instrument setup for TD DO is made up of picosecond pulsed lasers as light sources, Photomultiplier Tubes (PMTs) for light detection, and TCSPC boards for photon timing. TCSPC boards are high temporal resolution acquisition systems, usually expressed by

the average width of the time scale bins, *i.e.* the Least Significant Bit (LSB) (*e.g.*, <10 ps), and with a limited non-linearity of the time scale (*e.g.*, <0.02 LSB peak-to-peak) [3]. Though, their high cost (*e.g.*, >8 k€/unit) usually restricts to some units their use in instrument configurations and makes multi-channel setups expensive. Moreover, the TCSPC technique limits the maximum detected photon count rate, *i.e.* data throughput, to few percentages of the laser repetition rate to avoid signal distortion, thus forcing to an increase in the acquisition time to compensate for the low detection rate. PMTs can provide narrow time response function down to 30 ps FWHM depending on type and wavelength, but they are bulky, fragile, expensive (*e.g.*, >5 k€/unit) and extremely sensible to excess light exposures. These drawbacks and the limited options for parallelization due to high costs are the main limitations of the state of the art TCSPC detection chain.

The TD approach is well suited for one of the common applications of DO: the imaging and spectroscopy of the breast, *i.e.* Optical Mammography (OM). OM has been widely studied for the characterization of breast tissue and the identification of breast lesions, thanks to its sensitivity to physiological parameters altered by the presence of unhealthy tissue and to the use of non-ionizing health-safe radiation in the visible light spectrum and Near-Infrared (NIR) light spectrum (from 630 nm to 1100 nm) [1,4–6]. Further novel promising application fields are gaining interest in the scientific community, like the monitoring of neoadjuvant chemotherapy and prediction of its pathologic outcome, as well as the assessment of risk for breast cancer development [4,6–9]. OM could thus contribute to optimizing screening/diagnostic paths as well as treatment design, increasing patients' survival rate and improving their quality of life.

TCSPC is a highly informative TD technique and some implementations for OM can be found in literature [10–12]. Still, its limitations in terms of costs and low signal level (and subsequent long breast measurement time and potentially increased distress of the patient) could affect the future realization of a cost-effective and robust, commercial Optical Mammograph.

With our 7-wavelength (635-1060 nm) TD optical mammograph [11], during clinical studies involving more than 200 patients [13–15], we experienced limited signal level especially for thick and dense breasts at 1060 nm, due to strong tissue absorption combined with the limited available laser power and low detection efficiency, leading to small signal-to-noise ratio that could negatively affect data quality. Therefore, we decided to redesign the detection chain, employing new technologies for both photon detection and timing to improve light harvesting and data robustness.

Preliminarily, we identified some primary requirements that the new detection chain should fulfil for optimal use in OM:

- 1) spectrally extended sensitivity to cover the whole absorption spectrum of the main breast constituents in the “physiological window”: from the “red-light” region (VIS: 600–800 nm), where most of the information about hemoglobin resides, to the NIR region (up to more than 1 μm), where water, lipids and collagen are main tissue absorbers;
- 2) high sensitivity to compensate for the strong signal attenuation, especially at wavelengths >900 nm, where light absorption from water is strong;
- 3) high throughput for a robust quantification of tissue optical properties and composition, yet with limited measurement times;
- 4) intrinsically parallel or scalable configuration to easily produce a high coverage area probe at limited cost;
- 5) insensitivity (at least robustness) to abrupt signal changes (*e.g.*, near the border of the compressed breast, where tissue thickness reduces);

- 6) suitable temporal resolution (of the order of few hundred picoseconds);
- 7) cost-effectiveness.

These requirements could potentially be satisfied using Silicon Photomultipliers (SiPMs) as detectors and Time-to-Digital Converters (TDCs) as acquisition systems [16]. Both technologies are intrinsically cheaper and several SiPMs can be stacked in a very small volume as compared to PMTs, fostering the realization of multi-channel TD setups. Moreover, it has recently been demonstrated that in various situations high quantum efficiency SiPMs could successfully replace PMTs [17,18] and TDCs could replace TCSPC boards [19] for high throughput data collection.

Therefore, here we propose a complete detection chain for OM, based on 8 commercially-available SiPMs (stacked in a single custom-made probe to form a wide area detector) and a commercial multi-channel TDC, with overall high throughput and high sensitivity performances. The proposed detection chain is presently mounted on our Optical Mammograph and could be easily adapted to different DO applications where multi-channel (*i.e.* multi-position) systems are needed, *e.g.* brain activation monitoring.

We first provide a description of the single elements of the detection chain, followed by its characterization (through the Basic Instrument Performance assessment protocol, BIP [20]) in terms of diffuse optical responsivity, non-linearity of the timing electronics, and shape of the Instrument Response Function (IRF). Finally, we used homogeneous phantoms to carry out an application-driven performance assessment protocol, (mimicking the bulk characterization of the breast optical properties) *i.e.* the MEDPHOT protocol [21].

2. Materials and methods

2.1 The pre-existing instrument setup

Details on the layout of the pre-existing 7-wavelength TD optical mammograph and on its performances can be found in [11]. In this Subsection, a brief description is presented, to make the design of pre-existing and new elements as well as performance comparisons between them clearer, and to introduce the stand-alone system that has now been modified to include the new elements.

The instrument operates in transmittance geometry on the breast mildly compressed between plane parallel antireflection-coated laminated glass plates. It is mounted on wheels and suitable for use in a clinical environment. The compression unit can be rotated by an angle up to 90° in clock-wise and counter-clock-wise direction to acquire breast images in the cranio-caudal as well as medio-lateral or oblique views.

As shown in Fig. 1, 7 picosecond pulsed diode lasers emitting in the range of 635-1060 nm (*i.e.*, at 635, 680, 785, 905, 930, 975, and 1060 nm, LDH-P-XXX, PicoQuant, Germany, where XXX represents the nominal wavelength in nanometers) are used as the illumination sources, controlled by a single driver (PDL-808 “Sepia”, PicoQuant, Germany). The power at each of the 7 wavelengths can be adjusted independently by variable neutral density filters. Then, the 7 pulse trains are properly delayed through graded index optical fibers and coupled to a single injection optical fiber, followed by a lens producing a 5-mm diameter collimated beam that illuminates the breast. The full area of the compressed breast is raster-scanned moving in tandem the injection fiber and a 5.6-mm diameter collection fiber bundle. The distal end of the bundle is bifurcated and sends the collected pulses to two separate detection paths, depending on wavelengths: shorter (VIS) or longer (NIR) than 800 nm, respectively. Dedicated PMTs are exploited in the two spectral ranges (VIS: R5900U-01-L16, Hamamatsu, Japan; NIR: H7422P-60, Hamamatsu, Japan). Circular variable neutral density filters are placed in front of each PMT to control the illumination power, and the output signals of the detectors are amplified and input to two PC boards for TCSPC (SPC134, Becker&Hickl, Germany), which acquire the time-resolved transmittance curves at the 7 wavelengths.

The novel detection chain described in the following replaces the entire collection and detection paths, from the collection bundle on, as shown in Fig. 1.

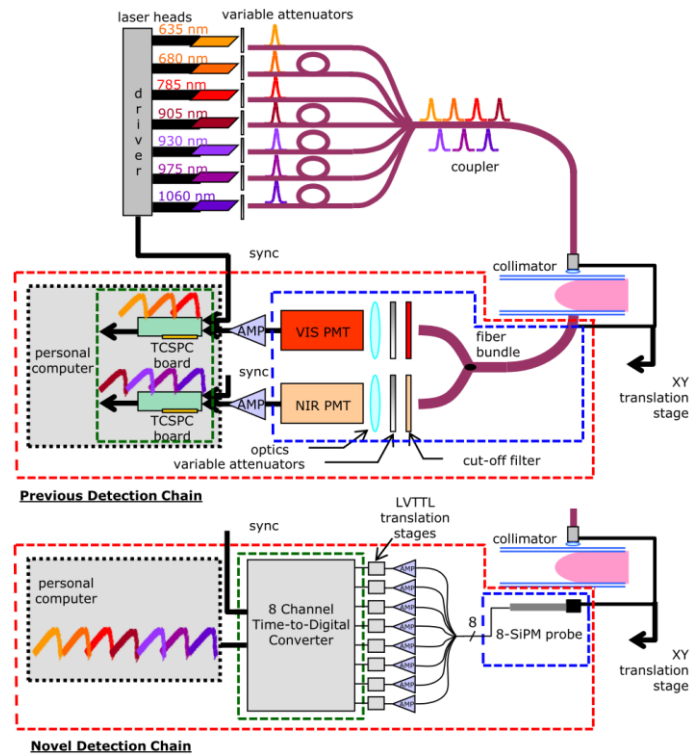


Fig. 1. Layout of the pre-existing instrument (top) and of the new detection chain (bottom). The red dashed line contours the set of components interested by the renewal process. The blue dashed line surrounds the detection elements and the green one the acquisition system.

2.2 The silicon photomultiplier (SiPM) probe

SiPMs are photon-number resolving detectors that can be used in the single-photon regime. They are composed of a matrix of up to thousands parallel microcells. Each cell is made up of a Single-Photon Avalanche Diode (SPAD) and a resistor for avalanche passive quenching and recovery [22]. The device exhibits a single global anode and a single global cathode where, all avalanche currents are summed up, and can therefore be used as a single detector.

Recently, SiPMs have been proposed as an alternative to the traditional detectors employed in TD DO applications [23–25]. SiPMs are (i) cheap and (ii) compact devices. Several of them can be stacked into a limited size probe, thus operating as a single macro-pixel detector, or they can be arranged to fabricate multi-channel TD DO systems. Their (iii) large active area, (iv) high numerical aperture, and (v) high quantum efficiency can be exploited to increase light harvesting efficiency. Their (vi) wide spectral coverage allows the use of a single detector to cover the range from 350 nm to 1100 nm. Moreover, (vii) they are not damaged by excess light illumination. Though, their single-photon timing response function shows a long tail (with nanoseconds decay time constant) that could limit the useful dynamic range and affect the retrieval of optical properties [23], especially the absorption contribution, mainly derived from long-time of flight photons (late photons). This is a well-known fingerprint of SiPMs operated as time-resolved single-photon detectors. Most probably, as occurring for SPADs, its origin is due to photons absorbed outside the high electric field region of the detector, where photo-generated carriers can only slowly diffuse before reaching the high field region, where they are eventually multiplied by impact

ionization, thus triggering a delayed avalanche of carriers. For this reason, the tail is often named “diffusion tail”. Moreover, their high dark count rate, up to hundreds of kilo-counts per second (kcps) could hide the weak TD signal.

Overall, the SiPMs’ features respond to most of the OM requirements, overcoming the main limitations of PMTs. Therefore, we developed an 8-channel SiPM probe, depicted in Fig. 2, using 8 commercially available SiPMs (model S13360-1350PE, Hamamatsu Photonics, Japan) to form a single macro-pixel detector. Each SiPM features a $1.3 \times 1.3 \text{ mm}^2$ active area, made of 667 pixels arranged with 74% geometrical fill factor. Each device is provided inside a surface mount package type, covered with transparent epoxy resin (refractive index 1.55). The package size is about $2.1 \times 2.6 \text{ mm}^2$. The 8 SiPM are soldered on a $1.0 \times 1.0 \text{ cm}^2$ custom-made Printed Circuit Board (PCB) in a squared pattern (as schematically depicted in Fig. 3) with a Negative Temperature Coefficient (NTC) resistor in the middle to measure the temperature of the devices. The average distance between adjacent active areas is about 1 mm due to the overall size of each individual package (exceeding the active area by 0.8 mm in one direction and 1.3 mm in the other one, due to the wire bonding pads needed to connect the SiPM die to the package contacts) and to the minimum distance of few hundred μm needed to mount the package on the PCB. In this way, the total actual active collection area is 10 mm^2 . The 8 devices are covered with a single $1.2 \times 1.2 \text{ cm}^2$ area protective glass capsule. A single-stage Thermo-Electric Cooler (TEC) device is mounted below the PCB: i) to stabilize the temperature of SiPMs to ensure a stable response over time, and ii) to slightly cool them below the room temperature (15°C) to limit the dark count rate. An external miniaturized microcontroller drives the TEC element. A 3D-printed black shield (see Fig. 2, center) surrounds the devices to avoid the detection of laterally impinging photons, which are usually due to stray light like room illumination. To further limit this effect, a high-pass gelatin filter (Kodak Wratten n° 25) was placed on top of the glass window and in contact with it to prevent the detection of photons at wavelengths shorter than 600 nm. The small PCB hosting the 8 SiPMs is mounted on top of a second custom-made PCB ($4 \times 3 \text{ cm}^2$), hosting the front-end circuit of each detector, which is needed to bias it and to read-out its faint avalanche signal (\sim few mV). This circuit is the passive network already proposed in a previous work to obtain suitable timing performance from the SiPM when operated in single-photon regime [17]. Eight thin radiofrequency coaxial cables, running along the probe holder, are used to connect the output signal of each SiPM front-end circuit to a custom-designed signal amplifier PCB. In this way, it is possible to obtain an amplified copy of the avalanche pulse with an amplitude of few tens of mV. Then, 8 custom-made signal conversion stage PCBs translate the amplified analog signals to standard Low-Voltage Transistor-Transistor Logic (LVTTTL) signals, which finally are provided to an 8-channel Time to Digital converter (see Subsection 2.3). These 8 LVTTTL conversion stage PCBs provide to the TDC voltage pulses with 23-ns time duration thanks a monostable multivibrator. Since the monostable cannot be retriggered until the output returns to the quiescence state, it features a dead time of 23 ns, which is larger than the dead time of each SiPM front-end (few ns, due to the need to recover the voltage baseline after each avalanche detection).

SiPMs are biased at 58 V, *i.e.* 6 V beyond the device breakdown to operate the detector in the so-called Geiger-mode, thus enabling the detection of single photons. The background noise of each detector is kept around 70 kcps thanks to the 15°C cooling temperature control and proper stray light shielding, as described above. The intrinsic jitter of each SiPM and front-end circuitry, evaluated as Full-Width at Half Maximum (FWHM) of the single-photon timing response function, is $130 \pm 5 \text{ ps}$ over the 600 – 1100 nm spectrum of interest for OM. The jitter of the external amplification and signal translation electronics is about 30 ps, and can therefore be neglected as compared to the SiPM jitter.

It is worth noting that the proposed probe has been designed to be directly used in front of the tissue under measurement (at a distance $\sim 1.1 \text{ cm}$ from the tissue mainly due to the compression plate thickness), with no need for optical fibers or focusing optics, thus

eliminating the related signal losses while probing a $\sim 2.3 \times 2.3 \text{ cm}^2$ tissue area. Furthermore, the proposed solution is inexpensive (overall $< 1 \text{ k€}$) as compared to typical PMTs ($\sim 5 \text{ k€}/\text{unit}$).

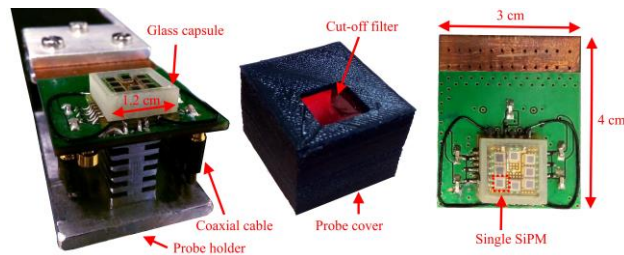


Fig. 2. The 8-channel SiPM probe (left) with the black shield that covers the probe during operation (center), and the detail of the PCB (right).

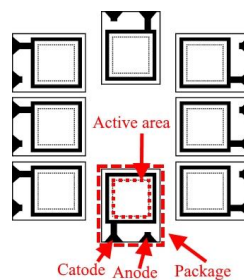


Fig. 3. Layout diagram of the 8-channel SiPM probe. The dotted line delimits the active area, and the dashed line the package.

2.3 The 8-channel time-to-digital converter (TDC)

In the proposed detection chain, a commercial 8-channel TDC (SC-TDC-1000/08 S, Surface Concept, Germany) acquires the timing signals from the SiPMs (STOP signals) and reconstructs the histogram of the photon distribution of time of flight (DTOF). The nominal temporal resolution, expressed by the average width of the time scale bins, *i.e.* the LSB, is on average 82 ps. However, the time scale is affected by a strong Differential Non-Linearity (DNL), that is a variation in the effective temporal width of the time bins, that is close to 1 LSB peak-to-peak, as characterized in Subsection 3.2. The temporal jitter of the device is represented by the uncertainty in the determination of a delta-like photon distribution and is assessed to be to $\sim 150 \text{ ps}$ (see Subsection 3.3).

The TDC measures the temporal delay between a START pulse triggered by the laser synchronization signal, and a STOP pulse provided by a photon hitting the SiPM detector. Due to the internal operation of the TDC electronics, the START signal should not exceed 7 MHz to provide proper timing. Therefore, an internal START Divider (SD) module is used to reduce the laser sync rate. Consequently, the effective time range spanned by the TDC for each START pulse is expanded by a factor of SD as compared to the inverse of the laser repetition rate, leading to a number of replicas of the DTOF curves as large as the SD factor. The replicas can be refolded (*i.e.*, superimposed) in order to improve the signal-to-noise ratio.

Over the 8 channels, the TDC can reach a maximum total throughput of 40 Mcps, limited mostly by the USB data transfer. Conversely, a typical TCSPC board reaches a saturated count rate of 10 Mcps, corresponding to the inverse of its internal dead time. In practice, a lower count rate must be chosen to avoid signal distortion. Operating the board at 50% of the saturated count rate (*i.e.*, at 5 Mcps max) with a random signal, a counting loss of about 50% is obtained [2].

The TDC has a low dead-time of ~ 5.5 ns, granting a low histogram distortion even under high count-rate, as studied in Subsection 3.5. At the same time, the cost per channel of the TDC used in the present study is one order of magnitude lower than the usual TCSPC boards.

In the following, we have used the commercial TDC, yet with original functions for refolding and correction of DNL (as reported in Subsection 3.2), and with a proper electronic stage for signal conversion to feed the TDC with LVTTTL pulses, as described above.

2.4 Measurement strategy and data analysis

The 7 wavelengths are pulsed at 10 MHz rate (100 ns period) and are time multiplexed so to be equally spaced by a factor of $100/7$ ns = 14.3 ns to fit all the 7 pulses in a 100-ns time window. To isolate only one wavelength, one can select the respective temporal region of interest or alternatively enable only the respective laser. Though, the analysis procedure is independent of the number of selected wavelengths. Each of the 8 SiPM detects all the 7 wavelengths within the same 100 ns time window. The DTOF curves from the 8 SiPMs are then aligned by the peak position and summed to increase the signal-to-noise ratio. The alignment is needed to compensate for the temporal shift each SiPM introduces arising from their squared spatial positioning.

Measured DTOF curves are convoluted with the IRF and then fitted with the theoretical curve obtained by solving the radiative transfer equation under the diffusion approximation for a homogeneous medium with extrapolated boundary conditions. The fitting range extends typically from 10% of the peak value on the raising edge to 10% on the falling edge of the curve. To retrieve the optical properties, the fitting procedure relies on the Levenberg-Marquardt algorithm to minimize the reduced χ^2 value.

3. Basic instrument performance assessment

To objectively and quantitatively assess the performances of the new detection chain, we adopted the Basic Instrument Performance (BIP) protocol, which is designed to verify the main hardware features of a TD DO system [20]. Since the focus of this paper is on the detection part, among the tests of the BIP protocol, we selected those related to the detection chain, which are: the diffuse optical responsivity (Subsection 3.1), the DNL of the timing electronics (Subsection 3.2) and the shape, background and stability of the temporal Instrument Response Function (Subsection 3.3).

3.1 Diffuse responsivity of the detection chain

The BIP Protocol defined a new figure, termed “*responsivity*” to quantify the overall detection efficiency of a diffuse optics detection system operated in single-photon regime. Light emerging from tissue after diffusive propagation can be modeled by a uniform Lambertian source with photon radiance L_p (in $s^{-1} m^{-2} sr^{-1}$). The *responsivity* of the detection system with respect to photon radiance is obtained from the count rate divided by the input photon radiance $s_{det}^L = (N_{det} / t_{meas}) / L_p$. Thus, the unit of the optical responsivity is easily determined to be $m^{-2} sr^{-1}$, visualized as an effective cross section in area and solid angle. This figure of merit is specific of diffuse optics instruments. It describes the detection chain as a “black box” and includes all possible factors contributing to the final yield in terms of number of counts (*i.e.*, detected photons), such as effective collection area, numerical aperture of the optics (including fibers), optical losses, quantum efficiency, thresholds and counting losses. In the following, to differentiate this new quantity from the classical electrical *responsivity* (A/W) of a detector, we term it *diffuse responsivity* ($m^{-2} sr^{-1}$).

Figure 4 shows the diffuse responsivity of the proposed detection chain (SiPMs and TDC) compared to the detection chain (PMTs and TCSPC boards) previously employed in our Optical Mammograph [11], measured at each of the 7 wavelengths used in the instrument. The decrease in diffuse responsivity at 785 and 1060 nm for the old detection chain is due to

the low quantum efficiency of the PMTs for the VIS and NIR range, respectively, at the long edge of their spectral sensitivity. The new detection chain achieves a minimum gain in diffuse responsivity of 70 at 933 nm, and a maximum of around 3100 at 1060 nm (average gain of 1000 on the full wavelength range of operation) as compared to the use of PMTs and TCSPC boards.

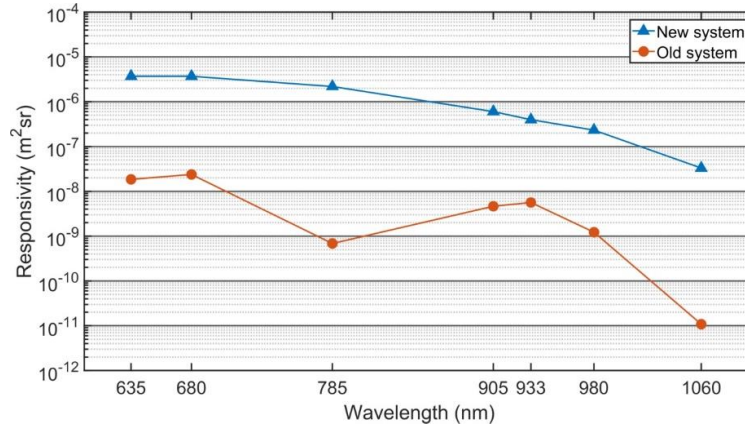


Fig. 4. Diffuse responsivity of the previous detection chain (red circles) and new detection chain (blue triangles) vs wavelength.

The SiPM detector can be placed close to the tissue, whereas the previous bulk detectors require a fiber bundle to collect the light transmitted through the breast. The active area of the new detector (10 mm²) is smaller as compared to the ~17 mm² active area of the fiber bundle, but it has higher Numerical Aperture (NA close to 0.8, limited by the black shield) with respect to the bundle (NA = 0.37). This contributes to the higher diffuse responsivity, which incorporates also losses introduced by the numerical aperture of collecting optics. Other contributing factors are the high quantum efficiency of the devices (>25% at 600 nm). Moreover, the low dead-time of the TDC (5.5 ns) as compared to the TCSPC board dead time (125 ns) reduces the number of related count losses at high count rates, improving signal detection.

3.2 Differential non-linearity (DNL) of the timing electronics

The DNL quantifies the deviation of the time bin duration of a TD system from the nominal value. Illuminating the detector with a signal uncorrelated to the synchronization signal (*e.g.*, a continuous signal coming from a battery powered lamp, to avoid electrical interferences) would lead to equal filling of the time bins of the acquisition system, *i.e.*, to a flat DTOF curve. Any distortion from this behavior is due to the DNL.

Figure 5(a) shows the recorded DNL of the TDC expressed in terms of LSB. The DNL of the i^{th} time bin is calculated as: $\text{DNL}_i = \frac{(n_i - \bar{N})}{\bar{N}}$, where n_i is the number of counts in the i^{th}

time bin and \bar{N} is the average number of counts that each time bin should ideally contain – if

they had all the same temporal duration – calculated as $\bar{N} = \frac{\sum_{i=1}^k n_i}{k}$, where k is the total

number of time bins. Each time bin contains $>10^5$ counts to provide a good signal-to-noise ratio. The DNL has a maximum measured value of 0.86 LSB peak-to-peak and significantly degrades the shape of the DTOF curve, as shown in Fig. 5(b) (red curve), potentially affecting the capability to retrieve the optical properties. A procedure for non-linearity compensation is therefore needed.

We implemented two different correction algorithms: one acts on the amplitude of the DTOF, while the other focuses on adjusting the time bin duration:

A) *Amplitude correction*. From the DNL distribution (Fig. 5(a)) we calculated the ratio between the number of counts in each time bin and the average value each bin would contain in case of ideal linearity. The ratios are then used to compensate for the real number of counts in each nominal time bin of the DTOF curve. In formulas: the ratio q_i (correction coefficient) calculated for the i^{th} time bin is given by $q_i = \frac{L_i}{\bar{L}}$, where L_i is the number of photon counts obtained with a battery powered (continuous signal) lamp, and \bar{L} is the average value over all the time bins. The correction is applied through the formula $\hat{n}_i = n_i / q_i$, where n_i is the number of counts in the i^{th} time bin and \hat{n}_i is the number of counts in the i^{th} time bin after the correction.

B) *Time bin correction*. From the DNL distribution we estimated the “true duration” of each time bin against the nominal value of 82 ps. A time scale with a fair smaller time bin (e.g., 24 ps) is defined and ratios between the “true duration” of each nominal bin and the new time bin duration are calculated. These ratios indicate the portion of counts each new time bin will contain with respect to the nominal one. The counts in each time bin of the DTOF curve are then distributed over the new time bins according to their “true” number of bins. In formulas: the ratio \hat{q}_i is the estimated true duration of the i^{th} time bin and is calculated as $\hat{q}_i = \Delta t \cdot q_i$ where Δt is the nominal time bin duration (i.e., 82 ps) and q_i is defined as above. We define a new linear time scale (i.e., with constant time bin duration) with a time bin duration $\Delta t \ll \Delta t$ (i.e., $\Delta t = 24$ ps). The number of photons in the j^{th} time bin of the linearized scale is: $\hat{n}_{j=1:l} = \frac{n_i}{\hat{q}_i} \cdot \Delta t$, where $l = \text{int}(\hat{q}_i / \Delta t)$. Then, if Δt is not an integer multiple of Δt , $\hat{n}_{l+1} = \frac{n_i}{\hat{q}_i} \cdot \text{rem}(\hat{q}_i / \Delta t)$. The correction is repeated until all the time bins of the new time scale are filled with the right number of counts.

We tested the correction algorithms on two figures of merit: (i) the residual DNL after correction, and (ii) the actual TDC temporal resolution achieved. The latter is evaluated as the recorded FWHM of a pseudo-Dirac delta signal: one branch of a split synchronization laser signal is used as the START signal and the other one is shortly delayed (~2.5 ns) and used as the STOP signal to the TDC. We applied the correction algorithms on 100 subsequent acquisitions of the pseudo-Dirac delta signal, measuring the average FWHM and the relative standard deviation to quantify also the reproducibility of the algorithm results. The results of the different corrections are summarized in Table 1.

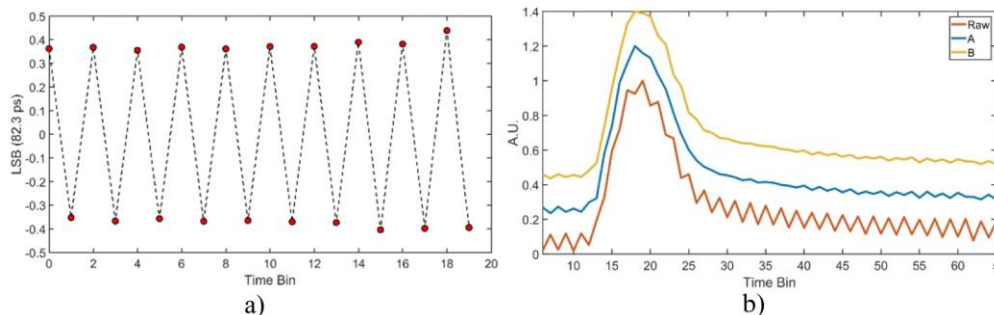


Fig. 5. a) Recorded DNL expressed in LSB. b) DNL effect on a DTOF raw curve (red) and the same curve processed with the proposed corrections A (blue) and B (yellow). The three curves are arbitrarily offset from one another for clarity.

Table 1. Performance of the correction algorithms^a

Method	Residual DNL (peak-to-peak)	Temporal Resolution
A	0.08	153 (20)
B	0.06	174 (24)

^aThe residual DNL is expressed in LSB units. The temporal resolution and

Both correction algorithms significantly reduce the DNL by a factor of 10. Since algorithm A produces the better resolution (153 ps) with lower standard deviation, it was implemented for following use.

3.3 Instrument response function (IRF)

The shape and FWHM of the IRF are strongly influenced by the laser pulse shape, by the temporal response of the detector, and the timing electronics. Here, we will focus mainly on the role of the temporal response of the SiPM detector.

In TD applications, it is often important to consider the shape of the trailing edge of the temporal IRF, since late photons provide most of the information on tissue absorption. Figure 5(b) shows temporal IRF of the system where the long-time constant of the trailing edge is ascribed to the SiPM temporal response, as discussed in Sect. 2.1 [23]. The trailing edge is composed of two exponential decay contributions: a fast decay with time constant of 65 ps, and a slow decay with time constant in the nanosecond range, starting 2 orders of magnitude below the peak. The latter contribution limits to about 2 decades the useful dynamic range where fitting analysis with theoretical models can effectively be performed.

The long-time constant could also cause an overlapping of DTOFs at high laser repetition rates, thus setting a limit to the maximum rate. Moreover, in the present instrument setup (*i.e.*, our optical mammograph), the 7-wavelength pulsed lasers sequentially emit at 10 MHz. Thus, the wavelengths are temporally separated by ~ 14.3 ns. To exemplify the situation, Fig. 6 shows the IRFs for 3 wavelengths, enabled one at a time, highlighting their overlapping. The dashed black line is the sum of the 3 different curves showing the realistic situation when the lasers are used together. The abrupt step that arises 23 ns after the rising edge of each IRFs is due the dead time of the LVTTL translation stage. Indeed, every time a given LVTTL translation stage is triggered by a given SiPM, all photon counts detected by the same SiPM within the following 23 ns are lost. Only photon counts detected after more than 23 ns by that SiPM can be processed by the detection chain. Therefore, this dead time gives rise to a loss of counts in the region of the IRF peak up to 23 ns, originating the step on the tail of the IRF when the operative condition of the LVTTL translation stage is restored. However, this distortion is out of the fitting region of the model employed for data analysis. This holds even when all wavelengths are on. Thus no additional error is introduced on the retrieved optical properties.

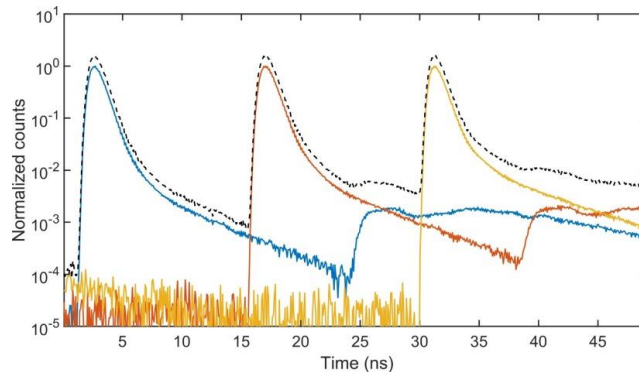


Fig. 6. Overlapping of the IRFs at 3 different wavelengths at 10 MHz laser repetition rate. The dashed black line (slightly shifted upward for clarity) is the sum of the 3 IRFs.

Overall, an IRF with temporal resolution of ~ 350 ps is obtained, given by the sum of the contributions of the SiPM ($\sim 130 \pm 5$ ps) and of the TDC ($\sim 150 \pm 20$ ps). The contribution of the SiPM is constant in the range of 635-1060 nm, as also reported in [23] for similar devices. The temporal resolution is lower than obtained with the previous detection chain using the PMT for the VIS range (180 ps for 635 nm, 680 nm and 785 nm wavelengths), but higher than the one obtained using the PMT for the NIR range (~ 400 ps for 905 nm, 930 nm, 975 nm and 1060 nm wavelengths). It is worth noting that the broadening of the DTOF curve due to photon diffusion through the tissue is usually in the order of few ns, much greater than the IRF width.

3.4 Stability

A high stability of the IRF in terms of shape, temporal resolution and total intensity is fundamental to ensure data quality and reproducibility of results during clinical measurements, and to provide sensitivity to small variations due to physiological changes in the breast during a diagnostic procedure or therapy treatment. An IRF was recorded every 2 min for 9 hr, measuring the integral number of counts N_{Tot} and the first moment $m_1 = \sum_{i=a}^b iN_i / N_{Tot} \cdot \Delta t$, where N_i is the number of counts in the duration Δt of the time bin of the histogram between the limits a and b (set to 1% of the maximum value). While N_{Tot} measures variations in laser power and detector efficiency, the first moment measures the timing drifts and jitter taking into account also the IRF shape, which would not be fully considered by the peak position [20]. Typical values of stability required for OM are few percentages variation in the IRF total intensity to produce good quality images, and fluctuations of the first moment within 10 ps to keep the time-shift-related error on reconstructed optical properties as low as 10% [26].

Figure 7 shows the results of the stability test for a single wavelength (*i.e.*, 975 nm) of the Optical Mammograph. Comparable results (data not shown) are obtained for the other wavelengths. The integral number of counts varies by $\sim 8\%$ in the first 4 hr, and thereafter the variation remains in the $\pm 0.5\%$ range. In 4 hr, the first moment reaches stability, within ± 5 ps range. The slow drift seen between the 7th and 9th hour is well within the expressed limits, and is acceptable considering the duration of a typical OM measure (~ 30 min).

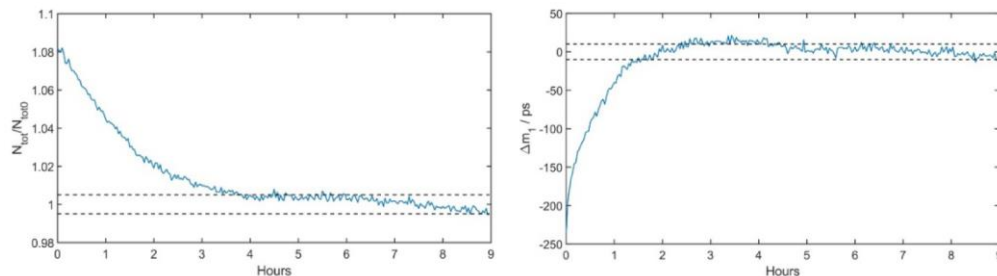


Fig. 7. Stability test on the IRF integral number of counts N_{tot} (left) and first moment m_1 (right). N_{tot0} is the average integral after the end of the warm up period (5-9 hr). The dashed lines indicate the ranges of $\pm 0.5\%$ (left) and ± 5 ps (right).

Thus, after a 4-hour warm-up period, the system reaches a good stability, suitable for the detection of physiological changes in breast tissue. The presence of a warm-up time few hours long can be attributed to the picosecond diode laser sources, and is in line with what obtained for similar instruments (and with the previous version of our mammograph, in particular).

3.5 Beyond the classical TCSPC limits

The classical rule of thumb for TCSPC techniques is to limit the maximum detected photon count rate to few percent of the laser repetition rate in order to reduce the pile-up distortion [2]. This effect arises from the loss of late-arriving photons due to the dead-time of the detectors and timing electronics triggered by early-arriving photons, thus causing the dumping of the tail of the DTOF curve, which can give rise to an overestimation of the absorption coefficient.

To compare the entity of pile-up distortions using the two acquisition methods (TDC and TCSPC board), we used the system mounting alternatively the TDC or the TCSPC board to retrieve the optical properties of a known tissue phantom (absorption coefficient $\mu_a = 0.1 \text{ cm}^{-1}$ and reduced scattering coefficient $\mu'_s = 10 \text{ cm}^{-1}$) at increasing count rate levels up to 30%, which is well beyond the classical rule of thumb for TCSPC operation. For both acquisition systems, we used the 8-channel SiPM probe as the detector and the laser repetition rate was set to 10 MHz. Figure 8(a) shows that, for the TCSPC board, the relative variation on the estimation of μ_a increases progressively up to 30% at the photon count rate of 30%. Instead, the trend for the TDC reaches a maximum variation of -3% , indicating reduced sensitivity to the relative count rate. The estimate of μ'_s , depicted in Fig. 8(b), follows the trend for μ_a , both for the TDC and the TCSPC board, probably due to a positive coupling effect. The coupling causes an overestimation of the reduced scattering coefficient in presence of high absorption, due to a dumping of the rising edge of the DTOF curve, which contains information mainly on the early scattered photons.

It appears that the TDC can overcome the limits of conventional TCSPC, thus exploiting a much higher photon detection count rate (up to 20-25% of the laser repetition rate to keep the quantification error below 10%), thus improving the overall signal level, and consequently the overall system throughput. The reason for this different behavior is still under investigation. The detection chain of the previous system based on PMTs and TCSPC boards has a dead time of 125 ns, due to the TCSPC electronics, while the new system based on SiPMs and TDC has a dead time of only 23 ns, due to the custom-made LVTTTL conversion PCBs. Therefore, the 5.5 ns dead time of the TDC is practically negligible. In principle, this should lead only to a different count loss due to photons impinging onto the detector when the timing electronics is not active. However, experiments clearly show a different trend in the relative error on the retrieved optical properties with the count rate, and this could be due to other effects. For instance, the 125 ns dead time is comparable to the time delay between two consecutive pulses of the same laser wavelength and, at high count rates, this can lead to distortions around the peak of the DTOF, where data are fitted to retrieve the optical properties, while the 23 ns dead time of the new detection chain produces a distortion, but out of the fitting region (see Fig. 6 and Subsection 2.4).

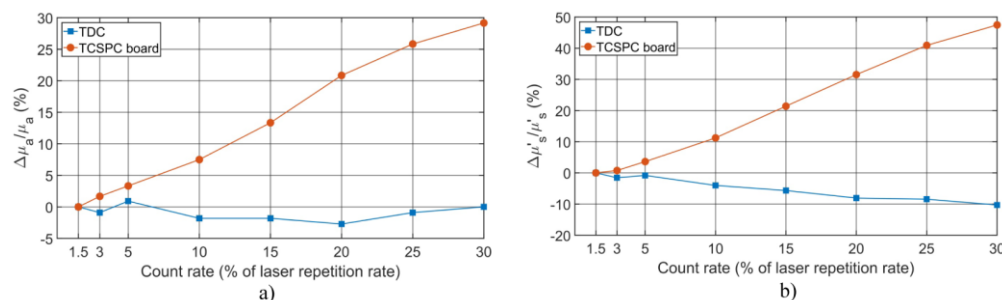


Fig. 8. Relative error vs relative count rate on the estimate of a) μ_a and b) μ'_s using the TCSPC board (red circles) and the TDC (blue squares). The laser repetition rate was 10 MHz.

4. Application-driven instrument performances: the MEDPHOT protocol

To validate the proposed detection chain for DO spectroscopy, we exploited the MEDPHOT protocol, which assesses the performances of photon migration instruments in retrieving the absolute values of the optical properties (absorption and reduced scattering) of homogeneous samples [21]. The protocol was applied on a kit of 32 homogeneous solid phantoms in transmittance geometry for all the 7 wavelengths of the instrument. The 4.5 cm-thick cylindrical phantoms cover a wide range of reduced scattering coefficients labelled with letters (A to D, nominally corresponding to $\mu'_s = 5, 10, 15, 20 \text{ cm}^{-1}$ at 800 nm) and absorption coefficients labelled with numbers (1 to 8, nominally corresponding to $\mu_a = 0 \text{ cm}^{-1}$ to 0.35 cm^{-1} , in steps of 0.05 cm^{-1} at 800 nm). It is worth noting that the nominal values for μ_a and derive from the phantom preparation stage, but their true value cannot be supposed to be μ'_s known accurately. So, instead we will use their conventionally true values derived from characterization through various independent measurements performed with TD DO spectroscopy setups [21]. We focused on the accuracy and linearity of the reconstructed optical properties.

Figure 9 shows the results in four graphs for the linearity test at 785 nm and 10 MHz laser repetition rate. Figure 9(a) and Fig. 9(b) highlight the system linearity for the absorption and reduced scattering measurements, respectively. Figure 9(a) shows the measured μ_a values ($\mu_{a,meas}$) against the conventionally true values ($\mu_{a,true}$). Similarly, Fig. 9(b) depicts the measured $\mu'_{s,meas}$ values against the $\mu'_{s,true}$ values. The presence of any coupling of $\mu'_{s,meas}$ to $\mu_{a,meas}$ is investigated in Fig. 9(c) and vice-versa in Fig. 9d. Linear interpolations (straight lines) are calculated from the first four points of the series. The legends in the figures report the conventionally true values for μ_a (Fig. 9(b) and Fig. 9(d)) and μ'_s (Fig. 9(a) and Fig. 9(c)).

The proposed detection chain is linear in absorption (Fig. 9(a)) up to $\mu_a \leq 0.2 \text{ cm}^{-1}$. Then the linearity starts to decrease reaching a maximum shift (*i.e.*, integral non-linearity) from the linear trend of 30% for $\mu_{a,true} = 0.34 \text{ cm}^{-1}$. The system shows good linearity in scattering (Fig. 9(b)) with a negligible offset ($<0.6 \text{ cm}^{-1}$) for most of the series and a maximum integral non-linearity $<21\%$ for $\mu'_{s,true} = 11.7 \text{ cm}^{-1}$. The horizontal lines in Fig. 9(c) show a negligible scattering to absorption coupling for $\mu'_{s,meas} \leq 8 \text{ cm}^{-1}$. The coupling is present for larger $\mu'_{s,meas}$ values, but the deviations are limited to $\sim 17\%$ in the $0-0.34 \text{ cm}^{-1}$ $\mu_{a,true}$ range. The absorption to scattering coupling (Fig. 9(d)) is negligible up to $\mu_{a,meas} \leq 0.2 \text{ cm}^{-1}$, as shown by the almost horizontal trend lines. For greater absorption values, a small positive coupling arises that causes a 17% increase of μ_a in the range $2.9 \text{ cm}^{-1} \leq \mu_{s,true} \leq 11.7 \text{ cm}^{-1}$.

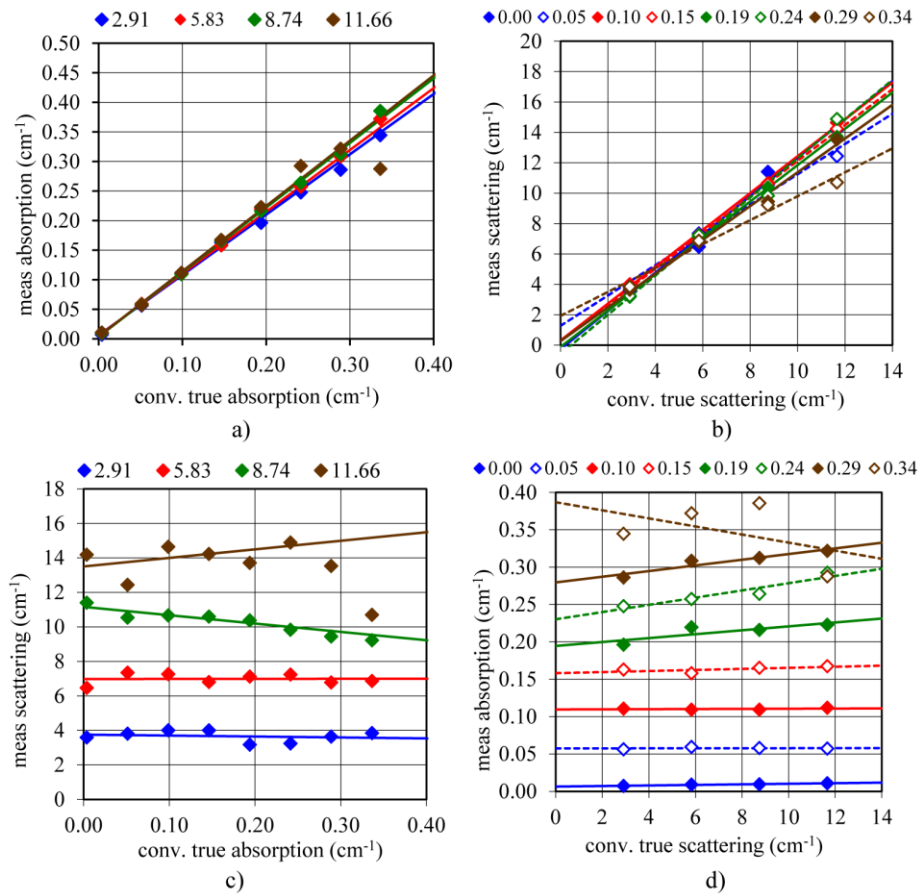


Fig. 9. Linearity plots reflecting the system linearity in a) absorption and b) scattering measurement; and coupling of c) scattering to absorption and d) absorption to scattering.

The accuracy test measures the relative error on the estimate of μ_a and μ'_s with respect to the conventional true values for the 32-phantom kit. Table 2 and Table 3 summarize the results. The estimate is overall better for μ_a than for μ'_s , when comparing the relative median of errors: 12% for the absorption and 21% for the reduced scattering. However, the reported errors are in agreement with results obtained with the previous system, and acceptable for real applications. The high relative error on μ_a for $\mu_{a,true} = 0.004 \text{ cm}^{-1}$ is mainly due to the difficulty of giving an accurate estimate of such a small absorption value. Even small positive offset values in the μ_a estimate, which are known to occur because of the Diffusion Approximation or of small experimental inaccuracies, will result in large relative errors because of the tiny value of the denominator (0.004 cm^{-1}) [27]. In practical cases, such low absorption values are never observed in breast tissue at red or near-infrared wavelengths (because of blood or water and lipid absorption, respectively).

More in general, the proposed detection chain has comparable performances to the previous system in terms of linearity and accuracy of the reconstructed absorption coefficient and reduced scattering coefficient of homogenous media. The long diffusion tail and the consequent superposition of different wavelengths do not significantly affect the estimation of the optical properties.

Table 2. Relative error on the estimate of μ_a^a

$\mu_{a,true}$	$\mu_{s,true}$			
	A	B	C	D
	(2.914)	(5.828)	(8.741)	(11.66)
1 (0.004)	93%	142%	152%	189%
2 (0.051)	10%	16%	13%	12%
3 (0.099)	12%	11%	11%	13%
4 (0.146)	11%	8%	13%	14%
5 (0.194)	1%	13%	11%	15%
6 (0.241)	3%	7%	9%	21%
7 (0.289)	-1%	7%	8%	11%
8 (0.336)	2%	11%	15%	-14%

Table 3. Relative error on the estimate of $\mu_s'^a$

$\mu_{a,true}$	$\mu_{s,true}$			
	A	B	C	D
	(2.914)	(5.828)	(8.741)	(11.66)
1 (0.004)	23%	11%	30%	22%
2 (0.051)	31%	26%	21%	7%
3 (0.099)	37%	25%	22%	26%
4 (0.146)	38%	17%	21%	22%
5 (0.194)	9%	22%	19%	18%
6 (0.241)	11%	24%	12%	28%
7 (0.289)	25%	16%	8%	16%
8 (0.336)	32%	18%	6%	-8%

^aThe numbers in bold are the conventionally true values for μ_a (phantoms 1–8) and μ_s' (phantoms A–D) in cm^{-1} units.

5. Conclusion

Time Domain Diffuse Optics applied to breast imaging and spectroscopy is often implemented by means of PMTs as detectors and TCSPC boards for photon timing. This leads to expensive and fragile instrument setups, often limited in signal, unsuitable for a clinical environment. Thus, to increase the signal level, we renewed the detection chain of our TD Optical Mammograph and proposed a cheaper, compact and robust alternative made by an 8-SiPM probe, forming a macro-area detector, and a multi-channel TDC. The new detection chain yields 2 to 3 decades higher diffuse optical responsivity and up to 10 times higher count rate with respect to the previous setup, while offering comparable performances in the estimation of optical properties as evaluated through the MEDPHOT protocol. These results were obtained despite a slightly higher level of DNL along with a less ideal temporal response of the SiPMs, with a slow time constant of the trailing edge that limits the IRF useful dynamic range to two decades.

The proposed detection chain thus positively answers the requirements for a valid TD detection chain for optical mammography. Work is now in progress to confirm the results achieved up to now with *in vivo* measurements, as a preliminary step in view of the system application in a clinical trial for the monitoring of neoadjuvant therapy.

Funding

European Union's Horizon 2020 research and innovation program under project SOLUS: "Smart Optical Laser and Ultrasound Diagnostics of Breast Cancer" (www.solus-project.eu, grant agreement No 731877). The project is an initiative of the Photonics Public Private Partnership.

Disclosures

The authors declare no conflicts of interest related to this article.